




LETTER TO THE EDITOR

## If you like C/O variations, you should have put a ring on it

Nienke van der Marel<sup>1</sup> , Arthur D. Bosman<sup>2</sup>, Sebastiaan Krijt<sup>3</sup> , Gijs D. Mulders<sup>4,5</sup> , and Jennifer B. Bergner<sup>6</sup> 

<sup>1</sup> Physics & Astronomy Department, University of Victoria, 3800 Finnerty Road, Victoria, BC V8P 5C2, Canada  
e-mail: [astro@nienkevandermare1.com](mailto:astro@nienkevandermare1.com)

<sup>2</sup> Department of Astronomy, University of Michigan, 323 West Hall, 1085 S. University Avenue, Ann Arbor, MI 48109, USA

<sup>3</sup> School of Physics and Astronomy, University of Exeter, Stocker Road, Exeter EX4 4QL, UK

<sup>4</sup> Facultad de Ingeniería y Ciencias, Universidad Adolfo Ibáñez, Av. Diagonal las Torres 2640, Peñalolén, Santiago, Chile

<sup>5</sup> Millennium Institute for Astrophysics, Chile

<sup>6</sup> Department of Geophysical Sciences, University of Chicago, Chicago, IL 60637, USA

Received 13 July 2021 / Accepted 30 August 2021

### ABSTRACT

**Context.** The C/O ratio as traced with C<sub>2</sub>H emission in protoplanetary disks is fundamental for constraining the formation mechanisms of exoplanets and for our understanding of volatile depletion in disks, but current C<sub>2</sub>H observations show an apparent bimodal distribution that is not well understood, indicating that the C/O distribution is not described by a simple radial dependence.

**Aims.** The transport of icy pebbles has been suggested to alter the local elemental abundances in protoplanetary disks through settling, drift, and trapping in pressure bumps, resulting in a depletion of volatiles in the surface layer and an increase in the elemental C/O.

**Methods.** We combine all disks with spatially resolved ALMA C<sub>2</sub>H observations with high-resolution continuum images and constraints on the CO snow line to determine if the C<sub>2</sub>H emission is indeed related to the location of the icy pebbles.

**Results.** We report a possible correlation between the presence of a significant CO-ice dust reservoir and high C<sub>2</sub>H emission, which is only found in disks with dust rings outside the CO snow line. In contrast, compact dust disks (without pressure bumps) and warm transition disks (with their dust ring inside the CO snow line) are not detected in C<sub>2</sub>H, suggesting that such disks may have never contained a significant CO ice reservoir.

**Conclusions.** This correlation provides evidence for the regulation of the C/O profile by the complex interplay of CO snow line and pressure bump locations in the disk. These results demonstrate the importance of including dust transport in chemical disk models for a proper interpretation of exoplanet atmospheric compositions and a better understanding of volatile depletion in disks, in particular the use of CO isotopologs to determine gas surface densities.

**Key words.** astrochemistry – molecular data – planets and satellites: formation – protoplanetary disks

## 1. Introduction

Elemental abundance ratios such as C/O and C/H are some of the most fundamental properties of the composition of protoplanetary disks and, as a result, of gas giant exoplanetary atmospheres (e.g., Madhusudhan 2019; Cridland et al. 2020). The C/O ratio in exoplanet atmospheres is considered a key measurement for linking the planet to its formation location in the disk. Whereas the classical view of an increasing step function in the disk at snow line locations (Öberg et al. 2011) has been expanded to a more advanced view due to pebble drift (Öberg & Bergin 2016; Booth et al. 2017; Krijt et al. 2020; Schneider & Bitsch 2021), the precise mechanisms leading to variations in C/O are still poorly understood (e.g., Bosman et al. 2021). Current disk surveys of C/O tracers such as C<sub>2</sub>H (Bergin et al. 2016; Semenov et al. 2018; Cleaves et al. 2018) appear to show a bimodal distribution of disks with and without C<sub>2</sub>H detection, indicating either high (C/O > 1) or low (C/O < 1) ratios (Bergner et al. 2019; Miotello et al. 2019), but it is unclear whether this bimodality is an intrinsic property or the result of physical-chemical processes. The recent discovery of low C/O at the location of the asymmetric Oph IRS 48 dust trap

(Booth et al. 2021a) suggests that pressure bumps may play a key role in regulating the C/O profile in disks, which is particularly relevant considering that pressure bumps are usually associated with giant planets (e.g., Pinilla et al. 2012b; van der Marel et al. 2016) and that those planets would accrete the composition of the gaseous material at the bump location. Pressure bumps act as dust traps, where large dust grains concentrate due to the gas-grain drag forces (e.g., Birnstiel et al. 2010), which results in the appearance of dust rings in continuum images of protoplanetary disks (Pinilla et al. 2012a). In this Letter the terms “dust ring” and “pressure bump” are used interchangeably, although dust rings without pressure bumps may also exist (e.g., Okuzumi et al. 2016; Vericel et al. 2021). The samples of the C<sub>2</sub>H surveys by Bergner et al. (2019) and Miotello et al. (2019) are biased toward brighter millimeter continuum disks, which are known to contain pressure bumps more often (Pinilla et al. 2020; van der Marel & Mulders 2021), as either ring disks (e.g., Andrews et al. 2018) or transition disks with inner cavities (e.g., Francis & van der Marel 2020). However, a clear correlation between C<sub>2</sub>H emission and dust substructure has so far not been identified (Bergin et al. 2016; Miotello et al. 2019; Bosman et al. 2021).

A connection between volatile composition and pebble transport has been previously suggested for infrared

\* Banting Research fellow.

line measurements of H<sub>2</sub>, CO, and H<sub>2</sub>O in TW Hya, by [Bosman & Banzatti \(2019\)](#), and for the anticorrelation of the H<sub>2</sub>O/HCN ratio of warm rovibrational lines and radial dust disk size, by [Najita et al. \(2013\)](#) and [Banzatti et al. \(2020\)](#). These authors pose a scenario where H<sub>2</sub>O vapor is elevated for the most compact disks where dust has drifted inside the H<sub>2</sub>O snow line, whereas disks with pressure bumps show lower or no H<sub>2</sub>O emission. The direct irradiation of the inner cavity wall may play an important role in particular in the desorption of oxygen-rich volatiles in transition disks ([Cleeves et al. 2011](#); [van der Marel et al. 2021](#)). Although dust rings are commonly detected in the brightest disks, they may actually not be that common in the total disk population ([van der Marel & Mulders 2021](#)): The selection bias of chemistry studies toward brighter disks could be a severe limitation in our understanding of the C/O in disks.

Interestingly, changes in the C/O ratio as a result of pebble transport may also reflect changes in the CO/H<sub>2</sub>, which is approximately a few times 10<sup>-4</sup> in the interstellar medium (ISM). In models that include pebble transport ([Öberg & Bergin 2016](#); [Krijt et al. 2020](#)), molecular CO is depleted by one to two orders of magnitude in the outer disk, which is indeed seen in spatially resolved CO isotopolog observations ([Schwarz et al. 2016, 2019](#); [Zhang et al. 2019](#)) and is shown to happen in the transition between the protostellar and the protoplanetary disk phase ([Zhang et al. 2020](#); [Bergner et al. 2020](#)). As the mixture of ices that are most affected by this depletion process (e.g., H<sub>2</sub>O, CO<sub>2</sub>, CO) is overall oxygen-rich, this process can result in outer disk surface layers with C/O > 1 in the gas phase ([Krijt et al. 2020](#); [Bosman et al. 2021](#)).

CO depletion can explain why CO isotopolog measurements of protoplanetary disks appear to result in very low gas masses ([Ansdell et al. 2016](#); [Miotello et al. 2017](#); [Long et al. 2017](#)), in particular in comparison with alternative gas measurements such as HD ([Bergin et al. 2013](#); [McClure et al. 2016](#)) and typical disk accretion rates ([Manara et al. 2016](#)). As the gas distribution in protoplanetary disks is fundamental for models of, for example, giant planet formation, disk evolution, and planet-disk interaction (e.g., [Helled et al. 2014](#); [Andrews 2020](#)), a better understanding of the effect of dust substructure on the volatile composition would also inform disk models used to infer gas masses from CO observations.

In this Letter we aim to study the connection between the C/O ratio in the gas in the outer disk, dust substructure, and pebble transport using a detailed analysis of the spatially resolved C<sub>2</sub>H profiles from the literature and the highest-resolution ALMA continuum images available for these sources. We focus in particular on the position of the CO snow line with respect to the dust rings as dust pebbles rich in CO ice are expected to drift inward to the nearest pressure bump and release the CO into the gas phase inside the CO snow line through sublimation, resulting in an enrichment of the CO abundance and restoring the C/O ratio to ~1. However, dust rings may be present either inside or outside the CO snow line, depending on their location and the brightness of the star. The aim of this study is to test if the combination of the stellar properties (and resulting CO snow line) and dust substructure regulates the radial C/O profiles in the disk.

## 2. Observations

Our sample consists of all protoplanetary disks with deep, spatially resolved C<sub>2</sub>H observations from the literature ([Bergin et al. 2016](#); [Bergner et al. 2019](#); [Miotello et al. 2019](#);

[Facchini et al. 2021](#)), primarily from the Atacama Large Millimeter/submillimeter Array (ALMA), and unpublished ALMA data of IRS 48. Most of these disks are observed in the 262.006 GHz C<sub>2</sub>H hyperfine doublet ( $N = 3 - 2$ ,  $J = 7/2 - 5/2$ ,  $F = 4 - 3$ , and  $F = 3 - 2$ ), and a handful in the 349.4 GHz doublet ( $N = 4 - 3$ ,  $J = 7/2 - 5/2$ ,  $F = 4 - 3$ , and  $F = 3 - 2$ ). The Miotello sample was selected from the brightest continuum disks in Lupus with a CO isotopolog detection and the Bergner sample from bright continuum disks, covering a range of stellar and age properties. We added three other disks: TW Hya ([Bergin et al. 2016](#)), PDS 70 ([Facchini et al. 2021](#)), and IRS 48 ([van der Marel et al. 2021](#)). For DM Tau, two published data sets exist, [Bergin et al. \(2016\)](#) and [Bergner et al. \(2019\)](#), and we chose to include the latter.

The disks were observed at a range of sensitivities and are located at distances between 60 and 175 pc, covering a range of stellar luminosity, spectral type, and age. The spatial resolution varies between 0.2'' and 0.8'', or at ~40 au spatial scale. The sample consists of 26 disks, with 20 C<sub>2</sub>H detections and 6 non-detections. The sample is listed in Table A.1.

For all disks, high-resolution continuum data at either 870 μm or 1.3 mm (ALMA Band 7 or 6) were taken with constraints on the dust substructure. Most continuum images have previously been published (references in Table A.1) and have a typical spatial resolution of 0.05'', or ~8 au. The images are shown in Fig. A.1 and cover a range of dust morphologies, including compact, ring, and transition disks. Compact disks are defined as disks without large-scale gaps, following [van der Marel & Mulders \(2021\)](#), transition disks as disks with a cleared inner dust cavity, and ring disks as disks with one or more gaps in the outer disk.

## 3. Analysis

In order to investigate the role of dust substructure on the presence of C<sub>2</sub>H, the C<sub>2</sub>H emission needs to be normalized spatially across the sample since the sample consists of disks of a range of sizes and the integrated flux (as used by the original studies) may not be representative. Therefore, we used the azimuthally averaged radial profiles of the integrated C<sub>2</sub>H emission and took the peak value as our main measurement of the C<sub>2</sub>H brightness, or the 3σ upper limit of the integrated emission in the case of a non-detection. As the doublet lines are blended, the integrated emission represents the integration over both lines. For the data in [Bergin et al. \(2016\)](#), [Bergner et al. \(2019\)](#), and [Facchini et al. \(2021\)](#), such radial profiles are provided. For the sample from [Miotello et al. \(2019\)](#), the azimuthally averaged profiles were computed from their zero-moment maps. All profiles are presented in Appendix B. For IRS 48, the C<sub>2</sub>H 349.4 GHz line upper limit was derived in Appendix C. In order to normalize the sample across spatial scales and beam sizes, the integrated peak flux density was converted to the brightness temperature and scaled to a distance of 100 pc. The resulting scaled peak brightness temperatures are listed in Table A.1.

The dust continuum images can provide a measurement of the amount of dust mass inside and outside the CO snow line. The latter provides a measurement of the amount of CO-ice-covered dust mass,  $M_{\text{dust,CO}}$  (i.e., the cold dust reservoir), which is hypothesized to dominate the regulation of the elemental abundance ratio. The CO snow line is defined as the location where the temperature (computed from the stellar luminosity) drops below 22 or 30 K, and the details of this calculation are provided in Appendix A. The  $M_{\text{dust,CO}}$  values are listed in Table A.1.

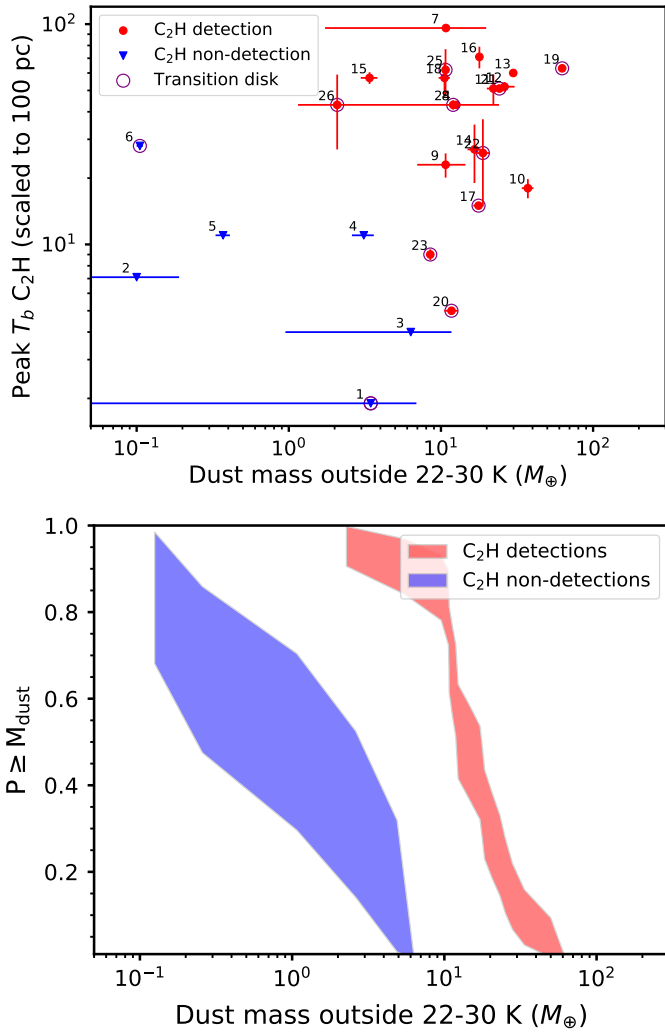


**Fig. 1.** Comparison between the scaled peak flux of the  $C_2H$  radial profiles and the millimeter-dust mass outside the CO snow line. The  $C_2H$  non-detections are indicated in blue, and these data points represent  $3\sigma$  upper limits. The  $C_2H$  detections are shown in red with  $1\sigma$  error bars. Transition disks are encircled. The numbers correspond to the targets as listed in Table A.1. Horizontally, the error bars indicate the range of dust masses for the chosen temperature of the CO freeze-out temperature (22–30 K), where the data point represents the average between these two values. The *bottom panel* shows the cumulative distribution function of the dust masses for the two groups, computed using the KME (see text). The two-sample tests indicate that although there is some overlap between the two samples, they are statistically distinct and the  $C_2H$  non-detection is possibly linked to the lower amount of CO-ice-covered millimeter dust in the disk.

## 4. Results

The disks with a  $C_2H$  non-detection have little or no dust emission outside the CO snow line (Fig. A.2), whereas all  $C_2H$  detections still have a significant cold dust reservoir. The CO snow line as determined by a temperature profile is a reasonable approximation, with the note that the measured CO snow line appears to lie farther out for the transition disks (suggesting a somewhat warmer temperature profile) and somewhat closer in for the ring disks, where available. Due to the lack of CO snow line measurements for the bulk of the disks, the dust mass outside the CO snow line can only be derived consistently throughout the sample using the temperature profile, with the caveat

that the dust mass may be somewhat underestimated for the ring disks and overestimated for the transition disks. For the transition disks, most dust rings lie at or outside the CO snow line, with the exception of IRS 48 and V4046 Sgr. For J16070854, the dust ring is difficult to identify due to the spatial resolution of the image, but visibility modeling indicates an inner cavity of  $\sim 40$  au (van der Marel et al. 2018).

The scaled  $C_2H$  peak brightness varies across the sample from  $<1.1$  up to  $97 \text{ K km s}^{-1}$ . The upper limits lie on the lower end of the detection values, but there is no obvious bimodal distribution as seen in the integrated flux (Miotello et al. 2019). The scaled  $C_2H$  peak temperature for PDS 70, V4046 Sgr, TW Hya, and IM Lup is at a similar level as the upper limits.

Using these properties, we now look for a dependence of the  $C_2H$  peak flux on the amount of icy dust mass in Fig. 1. The data points show the range of dust masses consistent with a CO snow line temperature of 22 to 30 K. As the dust emission is usually ring-like, the shift in the CO snow line temperature has a profound effect in some dust masses but is negligible in others, as can also be seen in the  $M_{dust,CO}$  values in Table A.1. Beam dilution is possibly affecting the estimates for the lower-resolution images, so some of these values may be upper limits. Figure 1 also shows the cumulative distributions of the disks with and without  $C_2H$  detection, using the Kaplan-Meier estimator (KME) from the ASURV package (Lavalley et al. 1992). The mean icy dust mass of the  $C_2H$ -detection group is  $18 \pm 3 M_\oplus$ , whereas the mean icy dust mass of the  $C_2H$ -non-detection group is  $2.0 \pm 0.9 M_\oplus$ .

For the scaled  $C_2H$  peak fluxes we computed a two-sample test using ASURV (to properly treat the upper limits of the  $C_2H$  data points). The Gehan Wilcoxon test (to include upper limits) indicates a probability of 0.5% that the two groups have been drawn from the same population. For the icy dust masses, this probability is 0.06%, so we can indeed conclude that the groups are statistically distinct. In order to check that this is not caused by an underlying correlation with another parameter, we performed a Kolmogorov-Smirnov statistic test for stellar luminosity  $L_*$  and total dust mass  $M_{dust}$ , and we find a probability of 92% for  $L_*$  and a probability of 23% for  $M_{dust}$  that the two groups have been drawn from the same distribution, so the difference is likely not caused by either of these properties. For the disk dust size (defined as the radius  $R_{68}$ , which encircles 68% of the total flux), this probability is 3.6%, so there could be an underlying relation there as well, although not as strong as with the icy dust mass, and the two parameters are obviously related.

## 5. Discussion and conclusions

The connection between the  $C_2H$  peak flux and the icy dust mass outside the CO snow line from Fig. 1 indicates a direct link between the C/O ratio and the presence of a CO-ice pebble reservoir. Such a reservoir requires millimeter dust at large radii, and hence the prevention of radial drift through pressure bumps outside the snow line. According to Krijt et al. (2020, Fig. 10), this results in a low CO abundance and elevated  $C/O \gtrsim 1$  in the surface layers in the regime outside the CO snow line, where the high C/O can be enhanced to  $\gtrsim 1.5$  as needed for a strong  $C_2H$  detection (Bergin et al. 2016) by additional vertical mixing and the destruction of carbonaceous grains (Bosman et al. 2021). Inside the CO snow line the CO abundance returns to the ISM value of  $10^{-4}$  and  $C_2H$  is below typical detection thresholds, which is consistent with the radial  $C_2H$  profiles (see Appendix B). The radial extent of  $C_2H$  is larger than the dust extent as the outer gas disk has been depleted by the settling and

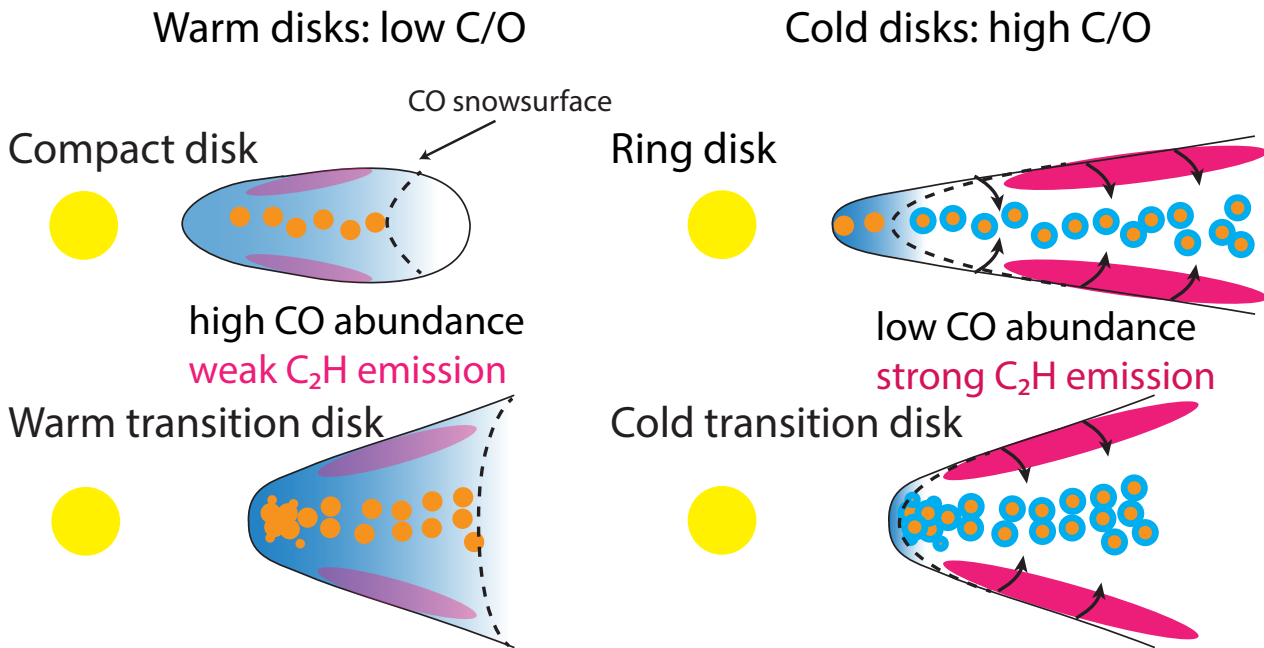


**Fig. 2.** Cartoon of the effects of dust transport in disks for different types of disks. Grain growth, settling, and vertical mixing drain volatiles from the outer disk atmosphere and lock them in grains in the midplane, leading to changes in  $C/O$  depending on the relative location of the snow line and the pressure bump. The  $C_2H$ -emitting region is indicated, where purple indicates weak emission and magenta strong emission. *Left:* warm disk with low  $C/O$  (low  $C_2H$ ). It could be either a compact dust disk without pressure bumps (and hence with efficient radial drift) or a transition disk with a dust ring (pressure bump) inside the CO snow line. In both cases the millimeter dust pebbles are not covered with CO ice. *Right:* cold disk with high  $C/O$  (high  $C_2H$ ). It could be either a ring disk or a transition disk with a dust ring (pressure bump) outside the CO snow line. As such, there is a large CO-ice dust reservoir, which depletes the surface layers of volatiles.

radial drift of icy dust grains. The observed lack of an anticorrelation between  $C^{18}O$  and  $C_2H$  by Bergner et al. (2020) is not at odds with this scenario, as they state that the  $C_2H$  production will not increase further with CO depletion when the  $C/O$  ratio is already elevated (Cleeves et al. 2018).

In contrast, the six disks with a  $C_2H$  non-detection contain little or no CO-ice-covered millimeter dust: In fact, four out of these six disks are compact in continuum emission and do not show any signs of substructure. The exceptions to this rule are IRS 48 and J16070384. IRS 48 has a bright, asymmetric dust trap, but this trap is located inside the CO snow line, unlike the other transition disks, whereas J16070384 shows a large edge-on dust ring but is overall very faint in millimeter dust.

If low  $C/O$  ( $C_2H$  non-detection) is indeed linked to the lack of CO ice, this suggests that these disks may have never contained a significant cold dust reservoir. This is indeed possible for the compact disks, under the assumption that the disks were warmer in the embedded phase and the pebbles drifted in before CO could freeze out. Faint CO emission in disks was recently suggested to be caused by these disks being compact and warmer (Miotello et al. 2021). In that case, the scenario of ice-covered pebbles drifting inside the CO snow line by Krijt et al. (2020) would not actually occur in disks. The detection of  $H_2CO$  and  $CH_3OH$  emission in IRS 48 (van der Marel et al. 2021) implies that this disk has either been cold enough to have had CO ice in the past or has inherited  $H_2CO$  and  $CH_3OH$  from the dark cloud phase (Drozdovskaya et al. 2014; Booth et al. 2021b) as  $CH_3OH$  ice sublimates at higher temperatures.

Other than IRS 48, the transition disks in this sample have their dust rings outside the CO snow line, implying that the bulk of the CO ice is not returned to the gas phase and that these transition disks are essentially the same as ring disks. The CO snow

line in transition disks may lie farther out than our estimates, as revealed by the direct measurements of the CO snow line of, for example, DM Tau and LkCa 15 (Qi et al. 2019). However, considering their radial profiles, this will not significantly decrease their icy dust mass to the level of the  $C_2H$  non-detections.

The four disks with low  $C_2H$  (IM Lup, TW Hya, PDS 70, and V4046 Sgr) may have a lower  $C/O$  ratio than the bulk of the  $C_2H$  detections, consistent with the derived value of  $C/O \sim 0.8$  from the detailed analysis of IM Lup (Cleeves et al. 2018). For TW Hya, Bergin et al. (2016) derived  $C/O \gtrsim 1$ , which may still be lower than the value of  $C/O > 1$  of the majority of the Lupus disks derived by Miotello et al. (2019). These four disks may fall in between the two extremes of the  $C/O$  ratios in our sample. Interestingly, all but IM Lup are transition disks. Transition disks are known to have irradiated cavity walls, with higher temperatures and different compositions of sublimated species (Cleeves et al. 2011; Bosman & Banzatti 2019).

Alternatively, there is a possible correlation between the dust disk radius and the  $C_2H$  brightness, which would suggest that the  $C_2H$  non-detections may just be caused by a smaller dust surface density area. Such a correlation could be understood if  $C_2H$  emission is primarily produced by the fragmentation of large grains that are mixed vertically into the hot surface layers, which is indeed predicted to be a contributing factor to  $C_2H$  (Bosman et al. 2021). However, such a relation would not be able to explain the low  $C/O$  in IRS 48. The current sample of available  $C_2H$  observations is not well constructed for fully testing our proposed scenario. Targeted, high-resolution observations of disks with pressure bumps inside and outside the CO snow line are needed.

In summary, this work suggests that the  $C/O$  value in disks (as traced by the  $C_2H$  emission) is related to the formation and



transport of CO-ice-covered dust pebbles. Figure 2 presents a summary of the proposed scenario. In large, cold ring disks the existence of a cold pebble reservoir results in a low CO abundance and a uniform high C/O ratio in the surface layers<sup>1</sup>. Alternatively, compact and/or warm disks do not efficiently sequester CO ice in the midplane and retain high CO and low C/O abundances at all radii. In general, the efficiency of CO-ice sequestration in the midplane depends on the interplay between dust coagulation, vertical settling, and turbulent mixing.

In transition disks, irradiation of cavity walls increases the desorption of ices (Cleeves et al. 2011, Fig. 2b), possibly lowering the gaseous C/O ratio to  $\sim 0.5$  farther out as the temperature gets high enough to desorb oxygen-rich ices. This means that the C/O ratio of giant planets inside the gaps is set by the complex interplay between pressure bumps and snow lines. If this hypothesis is correct, chemical disk models need to take dust transport and pebble history into account when analyzing CO and other molecular lines for proper interpretation, with a new potential of using CO isotopolog data to derive gas surface densities in disks. Using the current dust morphology, the effect of CO depletion due to dust transport can be estimated directly and used to set the CO abundance in the disk, which in turn can be used to derive gas surface densities.

This result is particularly timely as many spectra of exoplanet atmospheres are expected to be delivered in the coming years with, for example, the *James Webb* Space Telescope (JWST). As the exoplanet atmospheric composition and C/O ratio are set by the accretion of gas and icy pebbles, including gas released from the fragmentation of icy pebbles (Cridland et al. 2020), its formation history can only be interpreted when the C/O distribution in disks is properly understood.

*Acknowledgements.* We would like to thank the referee for their constructive comments which have helped to clarify the manuscript, and we thank Anna Miotello for useful feedback and Feng Long for the provided continuum data of the Taurus disks. N. M. acknowledges support from the Banting Postdoctoral Fellowships program, administered by the Government of Canada. G. D. M. acknowledges support from ANID – Millennium Science Initiative – ICN12\_009. ALMA is a partnership of ESO (representing its member states), NSF (USA) and NINS (Japan), together with NRC (Canada) and NSC and ASIAA (Taiwan) and KASI (Republic of Korea), in cooperation with the Republic of Chile. The Joint ALMA Observatory is operated by ESO, AUI/NRAO and NAOJ. This paper makes use of the following ALMA data: 2013.1.00198.S, 2013.1.00226, 2015.1.00671.S, 2015.1.00964.S, 2016.1.00627.S, 2016.1.00459.S, 2015.1.00888.S, 2017.A.00006.S, 2017.1.01167.S, 2017.1.00834.S, 2019.1.01619.S.

## References

- Andrews, S. M. 2020, *ARA&A*, 58, 483
- Andrews, S. M., Wilner, D. J., Zhu, Z., et al. 2016, *ApJ*, 820, L40
- Andrews, S. M., Terrell, M., Tripathi, A., et al. 2018, *ApJ*, 865, 157
- Ansdell, M., Williams, J. P., van der Marel, N., et al. 2016, *ApJ*, 828, 46
- Ansdell, M., Williams, J. P., Trapman, L., et al. 2018, *ApJ*, 859, 21
- Banzatti, A., Pascucci, I., Bosman, A. D., et al. 2020, *ApJ*, 903, 124
- Barenfeld, S. A., Carpenter, J. M., Ricci, L., & Isella, A. 2016, *ApJ*, 827, 142
- Bergin, E. A., Cleeves, L. I., Gorti, U., et al. 2013, *Nature*, 493, 644
- Bergin, E. A., Du, F., Cleeves, L. I., et al. 2016, *ApJ*, 831, 101
- Bergner, J. B., Öberg, K. I., Bergin, E. A., et al. 2019, *ApJ*, 876, 25
- Bergner, J. B., Öberg, K. I., Bergin, E. A., et al. 2020, *ApJ*, 898, 97
- Birnstiel, T., Dullemond, C. P., & Brauer, F. 2010, *A&A*, 513, A79
- Bisschop, S. E., Fraser, H. J., Öberg, K. I., van Dishoeck, E. F., & Schlemmer, S. 2006, *A&A*, 449, 1297
- Booth, R. A., Clarke, C. J., Madhusudhan, N., & Ilee, J. D. 2017, *MNRAS*, 469, 3994
- Booth, A. S., van der Marel, N., Leemker, M., van Dishoeck, E. F., & Ohashi, S. 2021a, *A&A*, 651, L6
- Booth, A. S., Walsh, C., Terwisscha van Scheltinga, J., et al. 2021b, *Nat. Astron.*, 5, 684
- Bosman, A. D., & Banzatti, A. 2019, *A&A*, 632, L10
- Bosman, A. D., Alarcón, F., Zhang, K., & Bergin, E. A. 2021, *ApJ*, 910, 3
- Chiang, E. I., & Goldreich, P. 1997, *ApJ*, 490, 368
- Cleeves, L. I., Bergin, E. A., Bethell, T. J., et al. 2011, *ApJ*, 743, L2
- Cleeves, L. I., Öberg, K. I., Wilner, D. J., et al. 2018, *ApJ*, 865, 155
- Cridland, A. J., van Dishoeck, E. F., Alessi, M., & Pudritz, R. E. 2020, *A&A*, 642, A229
- Drozdzovskaya, M. N., Walsh, C., Visser, R., Harsono, D., & van Dishoeck, E. F. 2014, *MNRAS*, 445, 913
- Dullemond, C. P., Dominik, C., & Natta, A. 2001, *ApJ*, 560, 957
- Facchini, S., Benisty, M., Bae, J., et al. 2020, *A&A*, 639, A121
- Facchini, S., Teague, R., Bae, J., et al. 2021, *AJ*, 162, 99
- Francis, L., & van der Marel, N. 2020, *ApJ*, 892, 111
- Helled, R., Bodenheimer, P., Podolak, M., et al. 2014, in *PPVI*, eds. H. Beuther, R. S. Klessen, C. P. Dullemond, T. Henning, et al., 643
- Hildebrand, R. H. 1983, *QJRAS*, 24, 267
- Krijt, S., Bosman, A. D., Zhang, K., et al. 2020, *ApJ*, 899, 134
- Lavalley, M., Isobe, T., & Feigelson, E. 1992, in *Astronomical Data Analysis Software and Systems I*, eds. D. M. Worrall, C. Biemesderfer, & J. Barnes, *ASP Conf. Ser.*, 25, 245
- Long, F., Herczeg, G. J., Pascucci, I., et al. 2017, *ApJ*, 844, 99
- Long, F., Herczeg, G. J., Harsono, D., et al. 2019, *ApJ*, 882, 49
- Madhusudhan, N. 2019, *ARA&A*, 57, 617
- Manara, C. F., Rosotti, G., Testi, L., et al. 2016, *A&A*, 591, L3
- McClure, M. K., Bergin, E. A., Cleeves, L. I., et al. 2016, *ApJ*, 831, 167
- Miotello, A., van Dishoeck, E. F., Williams, J. P., et al. 2017, *A&A*, 599, A113
- Miotello, A., Facchini, S., van Dishoeck, E. F., et al. 2019, *A&A*, 631, A69
- Miotello, A., Rosotti, G., Ansdell, M., et al. 2021, *A&A*, 651, A48
- Najita, J. R., Carr, J. S., Pontoppidan, K. M., et al. 2013, *ApJ*, 766, 134
- Noble, J. A., Congiu, E., Dulieu, F., & Fraser, H. J. 2012, *MNRAS*, 421, 768
- Öberg, K. I., & Bergin, E. A. 2016, *ApJ*, 831, L19
- Öberg, K. I., Murray-Clay, R., & Bergin, E. A. 2011, *ApJ*, 743, L16
- Okuzumi, S., Momose, M., Sirono, S.-I., Kobayashi, H., & Tanaka, H. 2016, *ApJ*, 821, 82
- Pinilla, P., Birnstiel, T., Ricci, L., et al. 2012a, *A&A*, 538, A114
- Pinilla, P., Benisty, M., & Birnstiel, T. 2012b, *A&A*, 545, A81
- Pinilla, P., Pascucci, I., & Marino, S. 2020, *A&A*, 635, A105
- Pinte, C., Ménard, F., Duchêne, G., et al. 2018, *A&A*, 609, A47
- Qi, C., Öberg, K. I., Andrews, S. M., et al. 2015, *ApJ*, 813, 128
- Qi, C., Öberg, K. I., Espaillat, C. C., et al. 2019, *ApJ*, 882, 160
- Schneider, A. D., & Bitsch, B. 2021, *A&A*, in press, <https://doi.org/10.1051/0004-6361/202039640>
- Schwarz, K. R., Bergin, E. A., Cleeves, L. I., et al. 2016, *ApJ*, 823, 91
- Schwarz, K. R., Bergin, E. A., Cleeves, L. I., et al. 2019, *ApJ*, 877, 131
- Semenov, D., Favre, C., Fedele, D., et al. 2018, *A&A*, 617, A28
- van der Marel, N., & Mulders, G. D. 2021, *AJ*, 162, 28
- van der Marel, N., van Dishoeck, E. F., Bruderer, S., et al. 2016, *A&A*, 585, A58
- van der Marel, N., Williams, J. P., Ansdell, M., et al. 2018, *ApJ*, 854, 177
- van der Marel, N., Booth, A. S., Leemker, M., van Dishoeck, E. F., & Ohashi, S. 2021, *A&A*, 651, L5
- van't Hoff, M. L. R., Walsh, C., Kama, M., Facchini, S., & van Dishoeck, E. F. 2017, *A&A*, 599, A101
- Vericel, A., Gonzalez, J.-F., Price, D. J., Laibe, G., & Pinte, C. 2021, *MNRAS*, 507, 2318
- Zhang, K., Bergin, E. A., Schwarz, K., Krijt, S., & Ciesla, F. 2019, *ApJ*, 883, 98
- Zhang, K., Schwarz, K. R., & Bergin, E. A. 2020, *ApJ*, 891, L17

<sup>1</sup> If some pebbles can filter through the pressure bumps, the direct vicinity of the CO snow line could see high gas-phase CO abundances and C/O  $\sim 1$ .

## Appendix A: Icy dust mass calculation

For our analysis we needed a measurement of the amount of dust mass outside the CO snow line, the icy dust mass, which we obtained using the continuum images presented in Fig. A.1. The CO snow line is known, based on observations, to be located at distances corresponding to a range of temperature values between 18 and 25 K (Pinte et al. 2018; Qi et al. 2019) and, based on laboratory work, is expected to be around 22 K for pure CO ice (Bisschop et al. 2006) or as high as 30 K for CO mixed in H<sub>2</sub>O ice (Noble et al. 2012). Attempts have been made to derive exact snow line locations in disks using snow line tracers such as N<sub>2</sub>H<sup>+</sup> and DCO<sup>+</sup>, but detailed 2D models have shown that their emission is more complex than a simple anticorrelation with CO (Qi et al. 2015; van't Hoff et al. 2017). Therefore, we adopted the 22 K and 30 K temperatures as the two extremes of the CO snow line location. For the temperature profile, we adopted the simplified expression of the midplane temperature in a passively heated, flared disk in radiative equilibrium (Chiang & Goldreich

1997; Dullemond et al. 2001):

$$T(r) = \left( \frac{\phi L_*}{8\pi\sigma_B r^2} \right)^{1/4}, \quad (\text{A.1})$$

with  $\sigma_B$  the Stefan-Boltzmann constant,  $\phi$  the flaring angle (taken as 0.02), and  $L_*$  the stellar luminosity. Using this equation, we can deduce the radius  $r_{\text{CO}}$  where  $T=30$  or 22 K in the midplane. For many of the disks in our sample, the CO snow line has been derived directly from the line data: Zhang et al. (2019) derived the snow lines of DM Tau, TW Hya, IM Lup, and HD163296 at  $\sim 12, 20, 30,$  and  $60$  au, respectively, which is consistently farther in than the 22 K line from the temperature profile from Eq. A.1. Qi et al. (2019) derived the CO snow line using detailed modeling of the N<sub>2</sub>H<sup>+</sup> emission profile for DM Tau, LkCa 15, and GM Aur at  $75^{+10}_{-30}, 58^{+6}_{-10},$  and  $48^{+10}_{-8}$  au, respectively, and set a limit of  $<33$  au for the V4046 Sgr system; the discrepancy for DM Tau may be due to the complex relation between N<sub>2</sub>H<sup>+</sup> and the snow line (van't Hoff et al. 2017). These values are all located farther out than our 22 K line, which is

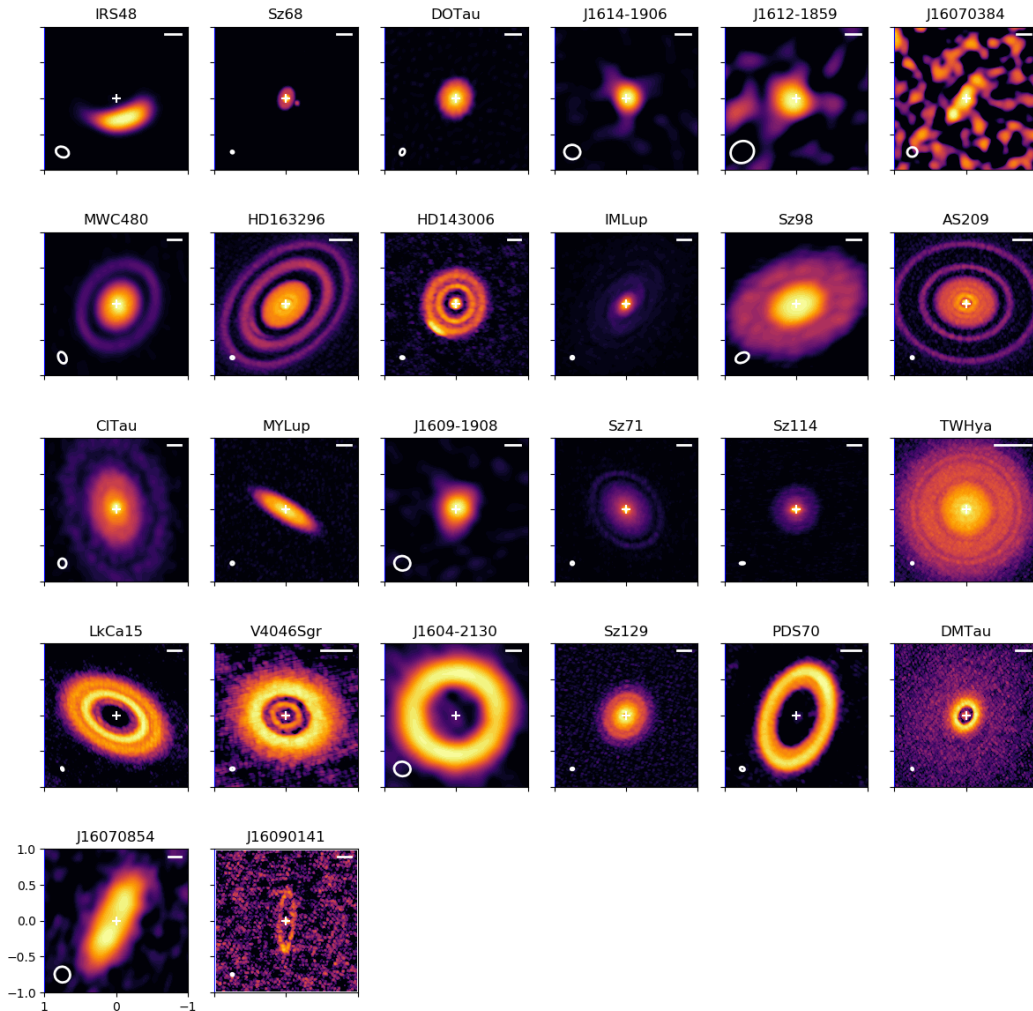


**Fig. A.1.** Continuum image gallery of the sources in our sample, shown with an asinh stretch. The beam size is indicated with a white ellipse in the lower-left corner. A bar in the top right indicates the 30 au scale. The top row shows the sources without C<sub>2</sub>H detection (mostly compact disks), followed by the disks with C<sub>2</sub>H detection: first the ring disks, followed by the transition disks, sorted by decreasing stellar luminosity.

expected as all these disks have large inner cavities where the temperature structure is altered due to the irradiation of the cavity wall (Cleeves et al. 2011). For the remaining targets, no CO snow line measurements are available in the literature.

Figure A.2 shows the normalized azimuthally averaged profiles of the dust continuum, with the temperature profile from Eq. A.1 and the corresponding 22-30 K range (expected CO snow line location) overlaid, plus the CO snow line derived directly, where available.

The continuum flux was computed by integrating the flux density over all pixels  $> 3\sigma$  outside  $r_{\text{CO}}$ , where  $\sigma$  is the rms noise. The corresponding dust mass was then computed using the standard assumptions of isothermal, optically thin emis-

sion of 20 K, as demonstrated by Hildebrand (1983) and regularly used in ALMA disk continuum surveys (e.g., Ansdell et al. 2016):

$$M_{\text{dust}} = \frac{F_{\nu, \text{CO}} d^2}{\kappa_{\nu} B_{\nu}(T_{\text{dust}})}, \quad (\text{A.2})$$

where  $B_{\nu}$  is the Planck function for a characteristic dust temperature ( $T_{\text{dust}}$ ),  $\kappa_{\nu}$  the dust grain opacity,  $d$  the distance to the target in parsecs, and  $F_{\nu, \text{CO}}$  the millimeter flux outside  $r_{\text{CO}}$ . Due to the lower spatial resolution of J1609-1908, J1612-1859, and J1614-1906, these icy dust masses should be considered upper limits.

**Table A.1.** Sample properties.

Target	Stellar		C <sub>2</sub> H line properties			Continuum properties						Refs <sup>b</sup>
	$L_{\star}$ ( $L_{\odot}$ )	$d$ (pc)	$F_{\text{integ}}$ (mJy km s <sup>-1</sup> )	$T_{b, \text{peak}, 100 \text{pc}}$ (K km s <sup>-1</sup> )	Beam (")	$F_{\text{total}}$ (mJy)	$\nu$ (GHz)	rms (mJy bm <sup>-1</sup> )	$M_{d < 30 \text{K}}$ ( $M_{\oplus}$ )	$M_{d < 22 \text{K}}$ ( $M_{\oplus}$ )	Beam (")	
1. IRS48	18	135	<11 <sup>a</sup>	<1.1 <sup>a</sup>	0.63x0.50	173	336	0.05	4.24	0.01	0.19x0.14	1,6
2. Sz68	5.5	154	<5.3	<7.1	0.25x0.21	76	239	0.02	0.19	0.01	0.04x0.03	2,7
3. DOTau	1.4	139	<62	<2.4	0.63x0.49	120	225	0.10	11.77	0.95	0.09x0.07	3,8
4. J1614-1906	0.5	143	<100	<5.3	0.56x0.45	20	239	0.04	3.62	2.60	0.22x0.20	3,9
5. J1612-1859	0.3	139	<97	<3.6	0.56x0.45	5.7	341	0.26	0.42	0.33	0.33x0.30	3,10
6. J16070384	0.25	150	<16	<24	0.25x0.21	0.5	225	0.04	0.11	0.10	0.13x0.12	2,11
7. MWC480	18.6	162	1846	97	0.73x0.47	264	225	0.06	20.0	1.7	0.17x0.11	3,8
8. HD163296	17	101	4396	41	0.55x0.47	634	239	0.02	24.1	1.1	0.05x0.04	3,7
9. HD143006	3.8	165	435	20	0.58x0.46	57	239	0.01	14.6	7.0	0.05x0.04	3,7
10. IMLup	2.6	158	1450	18	0.56x0.55	209	239	0.01	40.8	34.0	0.04x0.04	3,7
11. Sz98	1.53	156	1101	51	0.22x0.17	104	255	0.08	24.3	20.0	0.20x0.13	2,2
12. AS209	1.4	121	2709	52	0.65x0.55	233	239	0.02	30.6	21.9	0.04x0.04	3,7
13. CITau	0.9	159	1041	59	0.59x0.49	128	225	0.06	31.6	28.2	0.13x0.11	3,8
14. MYLup	0.87	157	284	27	0.22x0.17	78	239	0.02	18.4	14.9	0.04x0.04	2,7
15. J1609-1908	0.4	138	563	56	0.56x0.45	22	239	0.04	3.82	2.98	0.22x0.20	3,9
16. Sz71	0.33	156	1101	71	0.23x0.17	83	239	0.02	19.1	16.9	0.04x0.04	2,7
17. TWHya	0.3	60	10720 <sup>a</sup>	15 <sup>a</sup>	0.48x0.39	1380	346	0.03	19.2	16.3	0.03x0.03	4,12
18. Sz114	0.2	162	383	57	0.22x0.17	48	239	0.02	11.5	9.7	0.07x0.03	2,7
19. LkCa15	1.3	159	2435	62	0.59x0.49	229	341	0.02	24.1	24.1	0.05x0.03	3,13
20. V4046Sgr	0.86	72	2962	4.8	0.97x0.70	251	239	0.05	13.0	10.5	0.06x0.04	3,6
21. J1604-2130	0.7	150	2632	52	0.56x0.45	258	350	0.18	24.2	24.2	0.23x0.20	3,6
22. Sz129	0.44	162	107	26	0.26x0.21	82	239	0.02	20.9	17.0	0.04x0.03	2,7
23. PDS70	0.3	113	1327	8.7	0.39x0.32	159	351	0.03	8.5	8.5	0.07x0.05	5,7
24. DMTau	0.24	145	2013	43	0.57x0.49	56	225	0.01	12.0	12.0	0.03x0.02	3,7
25. J16070854	0.18	176	647	62	0.22x0.17	33	225	0.11	10.8	10.6	0.22x0.21	2,11
26. J16090141	0.15	164	200	37	0.25x0.21	7.6	225	0.02	2.1	2.1	0.04x0.03	2,14

<sup>a</sup> C<sub>2</sub>H  $N = 4 - 3$ ,  $J = 7/2 - 5/2$  doublet at 349.4 GHz rather than the  $N = 3 - 2$ ,  $J = 7/2 - 5/2$  doublet at 262.006 GHz. <sup>b</sup> References for the C<sub>2</sub>H data (first) and for the continuum data (second).

**Refs.** 1) This work; 2) Miotello et al. (2019); 3) Bergner et al. (2019); 4) Bergin et al. (2016); 5) Facchini et al. (2021); 6) Francis & van der Marel (2020); 7) Andrews et al. (2018); 8) Long et al. (2019); 9) ALMA archival data 2017.1.01167.S; 10) Barenfeld et al. (2016); 11) Ansdell et al. (2018); 12) Andrews et al. (2016); 13) Facchini et al. (2020); 14) van der Marel et al. in prep.

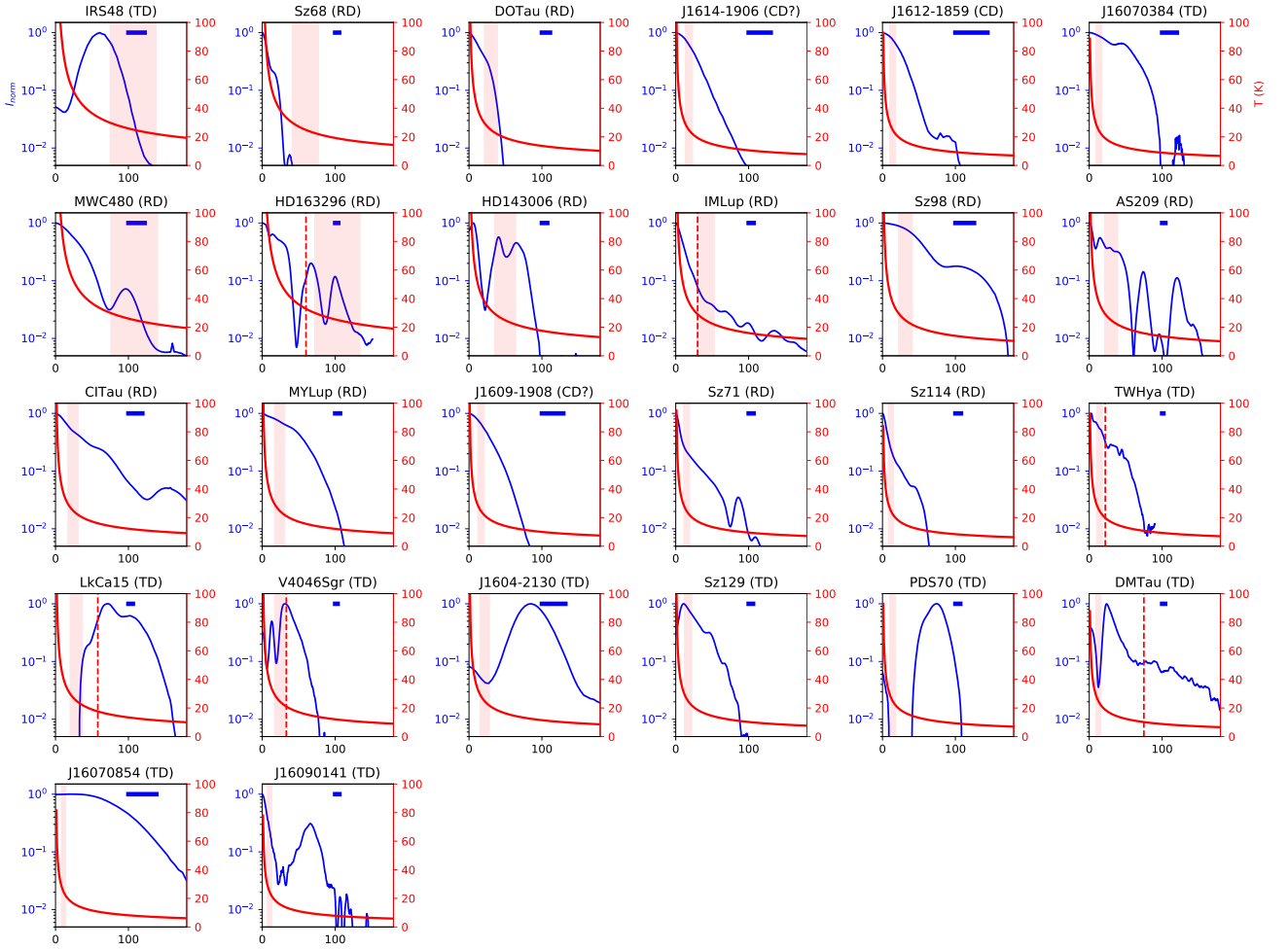


**Fig. A.2.** Azimuthally averaged and normalized intensity profiles of the dust continuum (blue) in combination with the temperature as computed from the stellar luminosity using Eq. A.1 (red). The transparent red bar indicates the 22–30 K temperature range (approximate CO snow line) according to this temperature profile. In some cases the CO snow line has been derived directly from observations (see text), which is indicated with a vertical dashed red line. A blue horizontal bar indicates the beam size. The top row shows the sources without  $C_2H$  detection, mostly compact disks (CD), followed by the disks with  $C_2H$  detection: first the ring disks (RD), followed by the transition disks (TD), sorted by decreasing stellar luminosity.



## Appendix B: C<sub>2</sub>H profiles

This section contains the radial profiles of the C<sub>2</sub>H emission from the zero-moment maps in the literature (Bergin et al. 2016; Miotello et al. 2019; Bergner et al. 2019; Facchini et al. 2021).

Although the spatial resolution of the C<sub>2</sub>H images is limited in current observations (Bergner et al. 2019; Miotello et al. 2019), the observed ring-like structures in their C<sub>2</sub>H zero-moment maps and the well-resolved TW Hya disk (Bergin et al.

2016) suggest that the C<sub>2</sub>H emission originates outside the CO snow line (Figs. B.1 and B.2). Centrally peaked C<sub>2</sub>H profiles such as those seen in CI Tau, J1609-1908, and LkCa 15 may just be the result of beam confusion and do not prove the presence of C<sub>2</sub>H inside the CO snow line. The C<sub>2</sub>H emission extends well beyond the radial dust extent, consistent with a gas disk much larger than a dust disk as icy dust pebbles settle and drift inward, leaving the outer disk volatile-depleted.

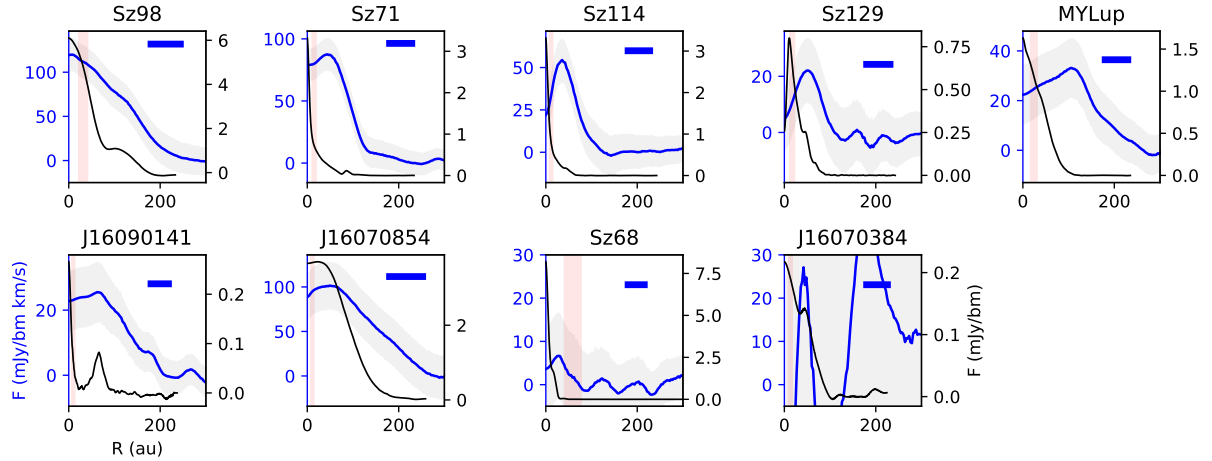


**Fig. B.1.** Radial C<sub>2</sub>H profiles of the Miotello sample (blue). The gray indicates the uncertainty. The CO snow line (in the 22-30 K range) is overplotted as in Fig. A.2, and the beam size is indicated as a blue bar in the top-right corner. The high-resolution continuum profiles of Fig. A.2 are overplotted in black to show that the C<sub>2</sub>H is always more extended than the continuum.

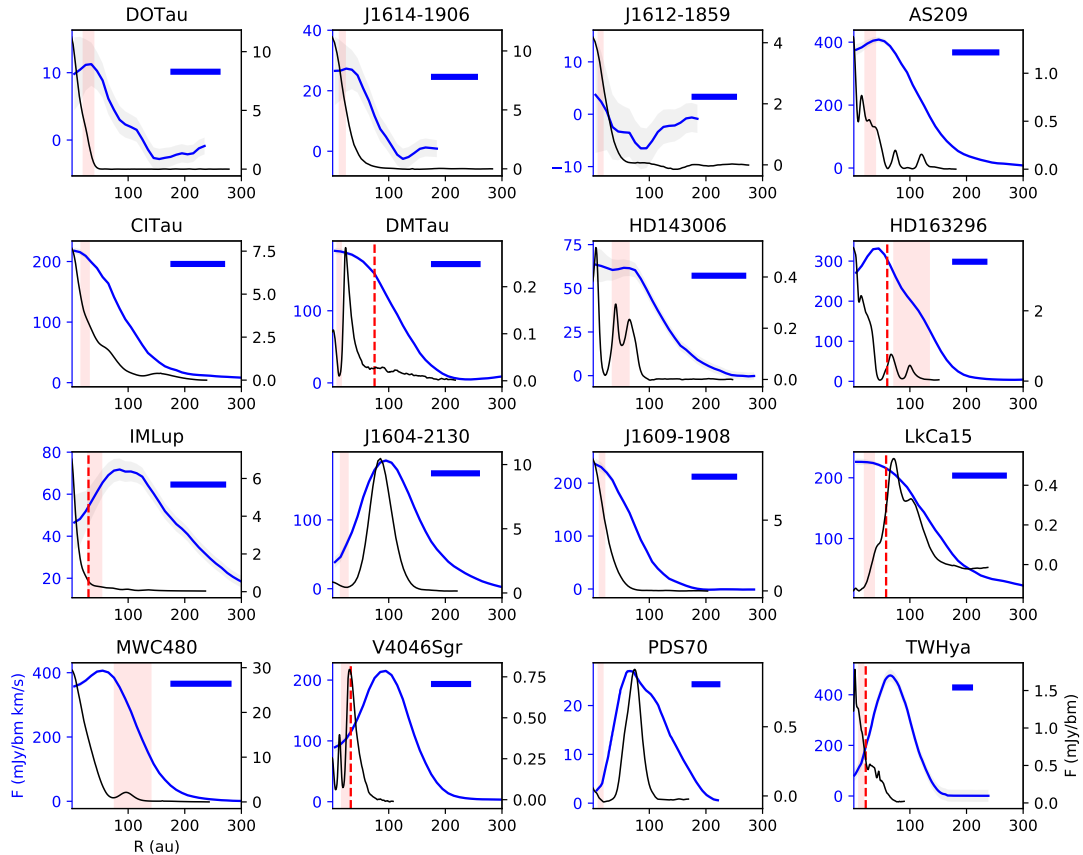


**Fig. B.2.** Radial C<sub>2</sub>H profiles (in blue) of the disks in the Bergner sample plus TW Hya (Bergin et al. 2016) and PDS 70 (Facchini et al. 2021). The gray indicates the uncertainty. The CO snow line (in the 22-30 K range) is overplotted as in Fig. A.2. The high-resolution continuum profiles of Fig. A.2 are overplotted in black to show that the C<sub>2</sub>H is always more extended than the continuum.

### Appendix C: Data reduction IRS 48 C<sub>2</sub>H data

van der Marel et al. (2021) present a molecular line survey of Oph IRS 48 from ALMA data set 2017.1.00834.S for a number of H<sub>2</sub>CO and CH<sub>3</sub>OH transitions. The C<sub>2</sub>H  $N = 4 - 3, J = 7/2 - 5/2$  doublet at 349.4 GHz is covered in these spectral windows as well but is not reported in this work. Inspection of the data set reveals that this C<sub>2</sub>H line is not detected. Considering the reported rms level of 1.2 mJy beam<sup>-1</sup> channel<sup>-1</sup> with a channel width of 1.6 km s<sup>-1</sup>, a line width of ~14 km s<sup>-1</sup>, and a beam size of 0.63×0.50" (van der Marel et al. 2021), we compute a 3 $\sigma$  upper limit on the C<sub>2</sub>H flux density of 11 mJy beam<sup>-1</sup> km s<sup>-1</sup>, or a scaled  $T_{b,peak,100pc}$  limit of <1.1 K km s<sup>-1</sup>. Such a low value of C<sub>2</sub>H is consistent with the low CS/SO ratio reported by Booth et al. (2021a).

### Appendix D: ALMA archival continuum data 2017.1.01167.S

For the continuum analysis of J1614-1906 and J1609-1908, we used ALMA archival data from ALMA Cycle 5 program

2017.1.01167.S (PI Sebastian Perez). These targets were observed in Band 6 for an integration time of 4.5 minutes each on January 18, 2018. The data set was reduced using CASA version 5.1.1 with the provided calibration scripts, with J1517-2422 as the flux and bandpass calibrator and J1634-2058 as the gain calibrator. We used the three continuum spectral windows (the fourth window was centered on the <sup>12</sup>CO 2–1 line) with an average frequency of 240 GHz and a total bandwidth of 6 GHz. The continuum images were imaged using the CASA `tclean` task with uniform weighting, resulting in a beam size of 0.22×0.20 and an rms noise of 0.08 mJy beam<sup>-1</sup>. The total integrated flux was 21 and 17 mJy for J1609-1908 and J1614-1906, respectively. Both disks are marginally resolved, and the CASA `uvmodelfit` indicates a radial extent of 0.14" (20 au) and 0.08" (11 au) for J1609 and J1614, respectively. Their disk morphology classification as compact disks is debatable due to the low resolution, and high-resolution imaging is required to properly assess these two disks. The images are presented in Fig. A.1.